

1-2013

# Nucleate boiling from smooth and rough surfaces - Part 2: Analysis of surface roughness effects on nucleate boiling

John P. McHale  
*Purdue University*

Suresh V. Garimella  
*Birck Nanotechnology Center, Purdue University, sureshg@purdue.edu*

Follow this and additional works at: <http://docs.lib.purdue.edu/nanopub>

 Part of the [Nanoscience and Nanotechnology Commons](#)

---

McHale, John P. and Garimella, Suresh V., "Nucleate boiling from smooth and rough surfaces - Part 2: Analysis of surface roughness effects on nucleate boiling" (2013). *Birck and NCN Publications*. Paper 1313.  
<http://dx.doi.org/10.1016/j.expthermflusci.2012.08.005>

This document has been made available through Purdue e-Pubs, a service of the Purdue University Libraries. Please contact [epubs@purdue.edu](mailto:epubs@purdue.edu) for additional information.



## Nucleate boiling from smooth and rough surfaces – Part 2: Analysis of surface roughness effects on nucleate boiling

John P. McHale, Suresh V. Garimella \*

Cooling Technologies Research Center, An NSF IUCRC, School of Mechanical Engineering and Birk Nanotechnology Center, Purdue University, West Lafayette, IN 47907-2088, USA

### ARTICLE INFO

#### Article history:

Received 21 February 2012

Received in revised form 30 July 2012

Accepted 9 August 2012

Available online 22 August 2012

#### Keywords:

Pool boiling

Nucleate boiling

Surface roughness

Characteristic length scale

ITO

Bubble nucleation

### ABSTRACT

The effect of surface roughness on nucleate boiling heat transfer is not clearly understood. This study is devised to conduct detailed heat transfer and bubble measurements during boiling on a heater surface with controlled roughness. This second of two companion papers presents an analysis of heat transfer and bubble ebullition in nucleate boiling with new measures of surface roughness: area ratio, surface mean normal angle, and maximum idealized surface curvature. An additional length scale of importance, the maximum base diameter of an emergent bubble, is identified. Measurements of bubble departure diameters, growth periods, ebullition periods, and void fraction above the surface are obtained from high-speed videographic visualizations by an automated procedure. Correlations of heat transfer coefficient and bubble ebullition characteristics with different measures of surface roughness are compared in terms of relative uncertainty. The data set of results for pool boiling in the perfluorinated dielectric liquid, FC-72, are found to correlate best with a length-scale filtered value of average roughness  $R_{a, \text{filt}}$ . Over a larger database with three different data sets including FC-72, FC-77, and water at atmospheric pressure, the most reliable correlations were obtained with the appropriately filtered area ratio. FC-72 bubble growth curves are well correlated for all test conditions with the normalized relationship  $D^* \sim (t^*)^{1/3}$ . Finally, the maximum void fraction in the region above the surface is correlated with normalized heat flux for these data and for water as the two-thirds power of heat flux.

© 2012 Elsevier Inc. All rights reserved.

### 1. Introduction

In Part 1 of this work [1], it was shown through a review of the literature that the effects of surface roughness on boiling heat transfer are not completely understood. Novel indium tin oxide (ITO) heater/sensor substrates with controllable surface roughness were therefore developed in order to measure boiling curves accurately and to exhaustively visualize bubble ebullition characteristics for surfaces with different roughness features. Quantitative and qualitative differences in boiling from smooth and rough surfaces were demonstrated. Boiling curves revealed that similar boiling curves do not imply similar  $R_a$  values, and similar  $R_a$  values do not imply similar boiling curves. Visualizations revealed that there is a marked difference in the bubble ebullition characteristics of smooth and rough surfaces. The inconsistent effect of  $R_a$  on the boiling curves and bubble behaviors suggests that the relative “roughness” of a surface should be quantified in a manner different from existing approaches to date in the literature.

Several recent studies have reported attempts to develop surface characterization methods that relate more directly to boiling

physics. Qi et al. [2] applied a digital “filtering” operation on 2-D surface scan data to examine potential nucleation sites in terms of cavity mouth radius and cone angle. They did not elaborate on the details of the algorithm; predictions of nucleation site density based on their analysis produced mixed results.

Methods of determining cavity sizes and locations directly from 2-D [3] and 3-D [4] surface scans using a rolling ball technique have also been proposed. In the latter, theoretical nucleation site locations were compared to those identified experimentally for pool boiling of propane from a copper tube. Results for number and distribution of active nucleation sites agreed qualitatively, but specific theoretical nucleation site locations did not match the experimental ones well.

Fractal analysis has been used to explain or reproduce surface roughness characteristics and nucleate boiling characteristics. Majumdar and Tien [5] first developed a fractal method for characterization of different machined stainless steel surfaces, achieving statistical similarity between real and simulated surfaces. Fong et al. [6] showed a correlation between the fractally derived surface roughness measure of a boiling surface and the critical heat flux (CHF). Yang et al. [7] achieved relatively good agreement between their simple fractal surface characterization and observed nucleation site densities in pool boiling of water on a stainless steel surface. Yu and Cheng [8] utilized nucleation site densities and

\* Corresponding author. Tel.: +1 765 494 5621.

E-mail address: [sureshg@purdue.edu](mailto:sureshg@purdue.edu) (S.V. Garimella).

## Nomenclature

$A$	vertical surface amplitude (m) Eqs. (7)–(9) planar area of bubble object in video (m <sup>2</sup> )	$z$	vertical height coordinate (surface analysis) (m)
$A_b$	planar base area (m <sup>2</sup> )	<i>Greek</i>	
$A_r$	area ratio (unitless)	$\alpha$	void fraction (unitless)
$A_s$	true surface area (m <sup>2</sup> )	$\phi_m$	surface mean normal angle, °, Eq. (5) or (6)
$a$	unknown constant	$\kappa_{max}$	idealized surface maximum curvature (m <sup>−1</sup> ), Eq. (10)
$b$	unknown constant	$\lambda$	surface wavelength
$c$	unknown constant	$\theta, \theta_r$	liquid contact angle (°)
$C_h$	heat transfer correlation constant, $h = C_h \cdot q^n$	$\Delta\rho$	density difference (liquid density–vapor density) (kg/m <sup>3</sup> )
$D$	bubble diameter (m)	$\sigma$	surface tension (N/m)
$g$	acceleration due to body force (m/s <sup>2</sup> )	$\tau$	bubble ebullition period (s)
$h$	boiling heat transfer coefficient (W/m <sup>2</sup> K)	<i>Subscripts</i>	
$i$	vertical counting index, Eq. (6)	0	value at intercept
$j$	horizontal counting index, Eq. (6)	base	value at base of bubble
$L_0$	Laplace length scale (m) $\sqrt{\sigma/g\Delta\rho}$	CHF	value at critical heat flux
$N$	sample size (unitless)	cut	cutoff
$m$	maximum vertical grid index, Eq. (6) surface roughness exponent, $h \sim R^m$	$d$	value at departure
$n$	maximum horizontal grid index, Eq. (6) boiling curve exponent, $h \sim q^n$	eq	equivalent
$p$	probability of Type-I error (unitless)	exp	experimental value
$q$	heat flux (W/cm <sup>2</sup> )	filt	filtered
$R_a$	average roughness (μm or m)	$m$	arithmetic mean
$R_p$	peak roughness (μm or m)	max	maximum
$R_q$	root-mean-square roughness (μm or m)	min	minimum
$R^2$	statistical coefficient of determination	ONB	value at onset of nucleate boiling/boiling incipience
$T$	temperature (K) (unless °C is specified)	pred	predicted value
$\Delta T$	temperature difference with respect to saturation (K or °C)	$w$	of heated wall
$t$	time coordinate in bubble growth (s)	<i>Superscripts</i>	
$V$	arbitrary variable, units by context	*	normalized quantity, or value for basis of comparison, Tables 3 and 4
$x$	lateral length coordinate (m)		
$y$	lateral width coordinate (surface analysis) (m) video height coordinate (bubble measurements) (m)		

bubble departure diameters predicted by fractal theory along with models for individual heat transfer mechanisms [9–14] to reproduce the experimentally observed boiling curves of Wang and Dhir [15] with good accuracy. Most recently, Sathyamurthi et al. [16] noted a similarity between the boiling curve and fractal dimensionality of the void fraction in contact with the surface in pool boiling. However, a widely applicable fractal approach has not been developed to date for the prediction of pool boiling heat transfer.

Prevailing theories of bubble nucleation and growth depend on the shape or at least the horizontal radius of the nucleating cavity.  $R$  values (single vertical roughness parameters, e.g.,  $R_a$ ,  $R_p$ ,  $R_q$ ) represent a single dimension of variation normal to the boiling surface. Fractal surface characterization depends upon at least two parameters, and the dimensionality of the measurement can be two or higher. The success of fractal surface characterization applied to boiling is probably due to the fact that the correlated parameters are more descriptive of the important features of the surface than conventional single linear measures.

In this paper, surface roughness is varied and carefully characterized and analyzed in terms of its relationship to bubble growth and departure. A new model for scaling surface roughness is proposed, as are alternative roughness measures that incorporate more physical underpinnings in preference to merely using  $R$  values. It is shown that the heat transfer results from the present work, as well as those of Jones et al. [17], are linearly correlated by a measurement of surface area ratio  $A_r$  obtained at an appropriate length scale. Correlations of measured bubble departure

diameters and times with the new length-scaled measure result in improved uncertainty compared to correlations with  $R_a$  or unscaled measures. Bubble measurements from the current work also suggest general relationships for bubble growth with time and for void fraction with heat flux in saturated pool boiling of FC-72.

## 2. Analysis of surface roughness

In the companion paper to this work [1], six borosilicate glass substrates were roughened by abrading with diamond compound to impart microscopic-scale roughness features, then annealed to control roughness characteristics at the nanoscale. One substrate (test piece 1) was not abraded or annealed. All seven substrates were coated conformally with an electrically conductive ITO layer, from which a 400 μm wide × 25 mm long heater/sensor device was patterned on each substrate. Each test piece was fixed at the base of a thermally controlled chamber that allowed saturated nucleate boiling heat transfer to be measured while recording high-speed videographic visualizations from beneath the test surface and from the side simultaneously.

Test pieces 4, 6, and 7 were abraded with the same diamond compound such that  $R_a$  values (and therefore microscopic-scale roughness features) would be similar. These three surfaces, however, were exposed to different annealing conditions of temperature and soak period as shown in Table 1 [1] such that the roughness characteristics at the nanoscale are very different. Boiling performance for the three surfaces differed as described

in [1], with higher wall superheats resulting from increased annealing time and temperature. Previous work [17] has demonstrated that the  $R_a$  (or  $R_p$  or similar) measurement is not sufficient to explain differences in boiling heat transfer coefficient for all cases, and in the present work, some extreme cases are presented. The two questions of interest are: (1) What is the length scale at which the roughness is most relevant to boiling? (2) Is a roughness parameter other than  $R_a$  a more appropriate measure?

### 2.1. Characteristic length scale model

During an ebullition cycle, bubbles may grow from a critical nucleus (with radius of order  $10^{-8}$  and  $10^{-6}$  m for conventional fluids at low to moderate reduced pressures) to an emergent bubble (with radius of order  $10^{-4}$ – $10^{-3}$  m), and even somewhat larger after multiple mergers near the surface. It is postulated that the roughness length scale of importance should depend, at a minimum, on: (1) fluid properties, and (2) the wetting characteristics of a particular surface–fluid combination. Fluid properties may imply some representative length scale (e.g., Laplace length), but this alone does not account for interactions between solid–liquid and liquid–vapor interfacial geometry. Conversely, a wetting characteristic such as contact angle, independent of fluid properties such as density and surface tension, is not sufficient to define an interface shape.

It is assumed here that interface shapes of individual emergent bubbles at moderate superheats are modeled well by a static analysis. Bashforth and Adams [18] calculated interface shapes for ebullient bubble and pendant drops acting under the influence of surface tension and a hydrostatic pressure gradient in terms rendered dimensionless through normalization by the Laplace length scale  $L_0 = \sqrt{\sigma/g\Delta\rho}$ . They considered static contact angle  $\theta$  as a parameter. Fritz [19] correlated the results of [18] for maximum contained volume as a function of  $\theta$  (units of  $^\circ$ ) as a simple relationship for departure diameter that reduces to

$$D_d = 0.0208 \cdot \theta \cdot L_0 \quad (1)$$

and is valid for contact angles up to roughly  $150^\circ$ . The Fritz departure diameter meets the criteria above, including fluid properties and wetting characteristic.

The Fritz departure diameter (225  $\mu\text{m}$  for the present study) is far too large, however, to explain the importance of the finer-scale roughness that has been demonstrated in the present work. A related length scale of physical significance is the contact diameter at the base of the maximal-volume bubble just prior to detachment. From the plots of Hartland and Hartley [20], who recomputed and expanded the results of [18], the following curve fit is obtained for the dimensionless base circle diameter of an emergent bubble as a function of contact angle:

$$D_{base}^+ \equiv D_{base}/L_0 = 2.194 \times 10^{-4} \cdot \theta^{1.937} \quad (2)$$

In Eq. (2),  $\theta$  is again expressed in degrees. The bubble remains attached to the surface during its entire growth period, and cannot remain attached to the surface beyond the corresponding maximum volume. Further, as the base circle diameter at maximum volume is almost identical to the maximum base diameter [20], the base circle diameter calculated from Eq. (2) is a useful maximum length scale of interaction between the surface and the bubble.

#### 2.1.1. Application of length scale-based filter

In order to isolate the surface features below the threshold length scale, a high-pass filter was utilized with cutoff wavelength  $\lambda_{cut} = D_{base}^+$  from Eq. (2). It was desirable to obtain a cutoff as smooth as possible in both the spatial domain and the frequency domain. A 1-D digital sinc filter [21] (which is low-pass, its

frequency response and kernel shown in Fig. 1a and b, respectively) was defined in MATLAB [22] using a Blackman window [23] of width large enough to prevent attenuation at zero frequency, but small enough to minimize ringing inherent to sharp cutoffs. The 1-D sinc filter was transformed to a 2-D radially symmetric filter kernel using the MATLAB command *ftrans2*(.). A z-data matrix, shown in Fig. 1c, was convolved with the filter kernel, resulting in a low-frequency representation of the surface, shown in Fig. 1d. The low-frequency z-data were subtracted from the original matrix, producing a high-pass filtered surface, as shown in Fig. 1e.

#### 2.1.2. Filtered vertical roughness parameters

After the filtering operation, new values of  $R_a$  for the test substrates were calculated by the method described in [1], and are listed in Table 2. For each surface, there was little to no difference between the values calculated for different interrogation window sizes; the lowest values are reported here. After the filtering operation, the average roughness values of surfaces 6 and 7 (abraded with 100- $\mu\text{m}$  particles and annealed more aggressively) fell below that of surface 3 (abraded with 30- $\mu\text{m}$  particles). Indeed, surface 7 appears to be similar in roughness to surface 2, which might be expected from the close proximity of their boiling curves.

### 2.2. Alternative measures of surface roughness

Unfiltered  $R_a$  values (or  $R_q$ ,  $R_p$ , etc.) cannot be directly related to cavity size or areal density, since they contain information about a single dimension ( $z$ ) only; but the filtered values should have improved correlation to cavity size and areal density, since the limiting wavelength is known.

Better measures are possible, however, if complete surface profiles are available. In the following paragraphs, some alternatives to  $R$  measures are proposed. It is shown later in this paper that these alternative definitions may offer better linear correlations than unfiltered  $R_a$  values. Values of each parameter to be introduced in Sections 2.2.1–2.2.3 for surfaces 1–7 before and after filtering are given in Table 2.

#### 2.2.1. Area ratio

The area ratio  $A_r$  is defined as

$$A_r \equiv \frac{\text{true surface area, } A_s}{\text{planar base area, } A_b} \quad (3)$$

which can be calculated from ( $x, y, z$ ) data on a rectangular grid to a suitable numerical approximation as:

$$A_r = \frac{1}{(x_{\max} - x_{\min})(y_{\max} - y_{\min})} \times \int_{x_{\min}}^{x_{\max}} \int_{y_{\min}}^{y_{\max}} \sqrt{1 + \left(\frac{\partial z}{\partial x}\right)^2 + \left(\frac{\partial z}{\partial y}\right)^2} dy \cdot dx \quad (4)$$

In the present work, calculation of Eq. (4) was accomplished through a double application of Simpson's 3/8 rule. Partial

**Table 1**  
Test substrate parameters.

Device No.	$d_{p,nom}$ ( $\mu\text{m}$ )	$T_{anneal}$ ( $^\circ\text{C}$ )	$t_{anneal}$ (min)	$R_a$ ( $\mu\text{m}$ )	$R_q$ ( $\mu\text{m}$ )
1	–	–	–	0.263	0.319
2	15	725	5	0.622	0.789
3	30	740	15	1.396	1.755
4	100	725	5	4.25	5.22
5	250	725	5	7.51	9.13
6	100	740	15	4.40	5.41
7	100	750	45	3.73	4.58

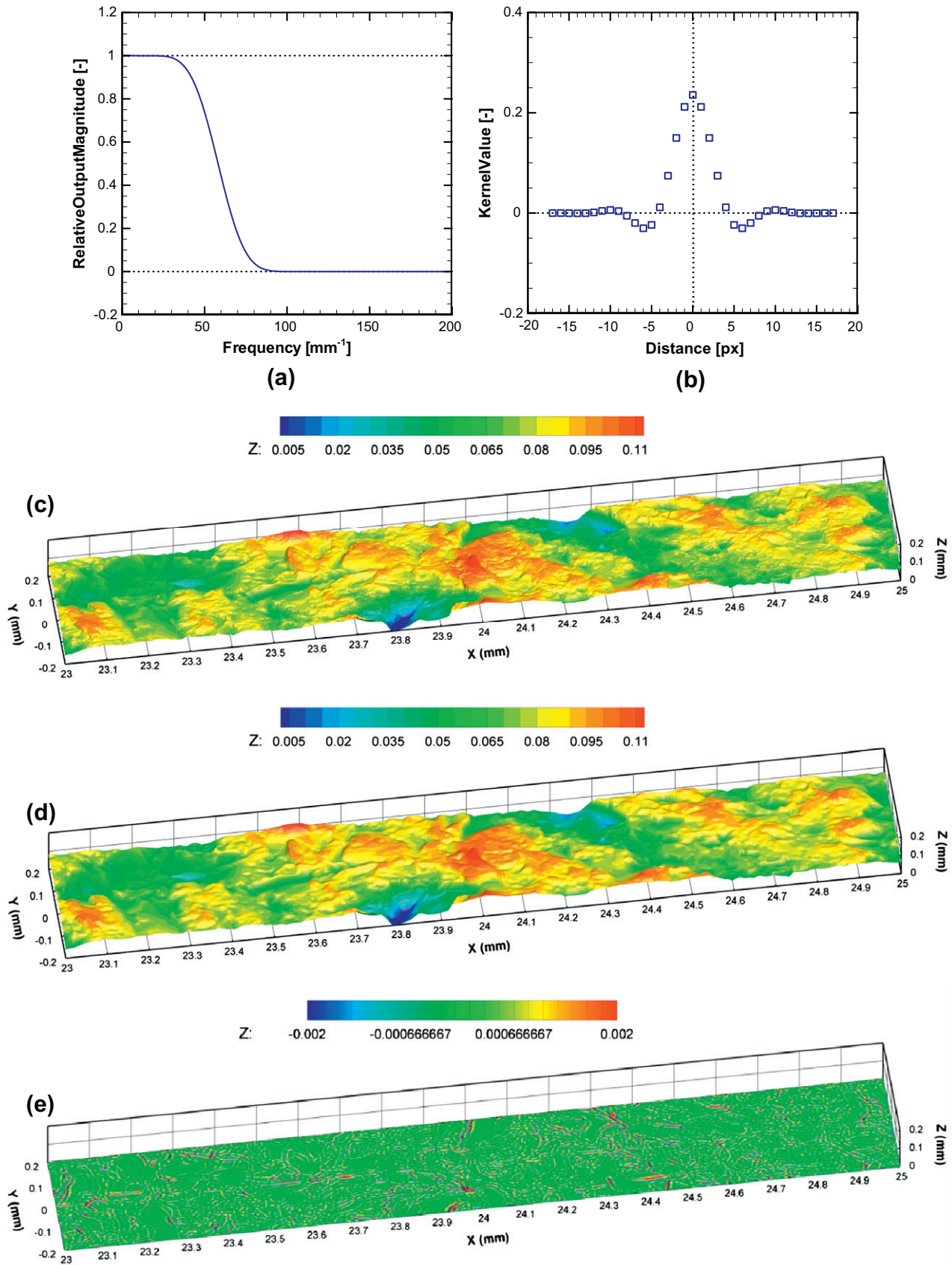


**Fig. 1.** Surface maps were filtered with cutoff frequency determined by the predicted bubble base diameter: (a) frequency response of the filter for FC-72, (b) Blackman-windowed 1-D sinc filter, (c) unfiltered section for surface 5, (d) surface 5 after low-pass filtering, and (e) high-frequency surface roughness features remaining after subtracting (d) from (c).



**Table 2**

Comparison of surface parameters before and after filtering (present data).

Substrate No.	$R_a$ ( $\mu\text{m}$ )	$R_{a, \text{filt}}$ ( $\mu\text{m}$ )	$A_r$ (–)	$A_{r, \text{filt}}$ (–)	$\phi_m$ ( $^\circ$ )	$\phi_{m, \text{filt}}$ ( $^\circ$ )	$\kappa_{\text{max}}$ ( $\text{m}^{-1}$ )	$\kappa_{\text{max, filt}}$ ( $\text{m}^{-1}$ )
1	0.263	0.0112	1.0007	1.0003	0.41	0.39	$1.91 \times 10^2$	$4.08 \times 10^3$
2	0.622	0.222	1.024	1.013	10.53	7.56	$5.55 \times 10^4$	$7.95 \times 10^4$
3	1.396	0.438	1.089	1.048	19.54	14.45	$9.01 \times 10^4$	$1.52 \times 10^5$
4	4.25	0.473	1.168	1.057	25.29	14.86	$5.25 \times 10^4$	$1.49 \times 10^5$
5	7.51	0.575	1.251	1.088	28.97	16.97	$4.08 \times 10^4$	$1.62 \times 10^5$
6	4.40	0.383	1.141	1.042	22.79	11.75	$4.01 \times 10^4$	$1.13 \times 10^5$
7	3.73	0.248	1.093	1.016	19.58	7.98	$3.39 \times 10^4$	$7.92 \times 10^4$

derivatives were approximated as two-point central finite differences, except at the edge of the grid where forward or backward differences were used instead. Values of  $A_r$  were calculated for surface maps before and after filtering and are given in Table 2. Physically,  $A_r$  is the dimensionless surface area, while  $A_{r, \text{filt}}$  is the normalized surface area for a given length scale  $\lambda_{\text{cut}}$ .

### 2.2.2. Mean surface normal angle

Further proposed is a new surface roughness parameter, the mean surface normal angle  $\phi_m$ , defined as

$$\phi_m \equiv \frac{1}{A_b} \iint_{A_b} \cos^{-1} \left[ \frac{\langle (1, 0, \frac{\partial z}{\partial x}) \times (0, 1, \frac{\partial z}{\partial y}) \rangle \cdot \langle 0, 0, 1 \rangle}{| \langle (1, 0, \frac{\partial z}{\partial x}) \times (0, 1, \frac{\partial z}{\partial y}) \rangle |} \right] dA, \quad (5)$$

which, for discrete  $z$  data on a regularly spaced  $m \times n$  ( $x, y$ ) grid, becomes:

$$\phi_m \equiv \frac{1}{m \cdot n} \sum_{i=1}^m \sum_{j=1}^n \cos^{-1} \left[ 1 + \left( \frac{\partial z}{\partial x} \right)^2 + \left( \frac{\partial z}{\partial y} \right)^2 \right]^{-1/2} \quad (6)$$

Values of  $\phi_m$  before and after filtering are given in Table 2. The effect of surface filtering on  $\phi_m$  is not nearly as great as its effect on  $R$ .

The mean normal angle parameter represents the average steepness of asperities on a surface, regardless of length scale. Just as  $R$  numbers alone provide no information about the density or horizontal size of cavities on a surface,  $\phi_m$  alone cannot provide information about the length scale of cavities. The parameter is qualitatively related, however, to the average cavity cone angle of a surface, and hence, to whether potential nucleation sites on a surface would tend to be active or flooded. Values of  $\phi_m$  can also be used along with amplitude measurements to determine average asperity wavelengths.

### 2.2.3. Derived quantities

An idealized sinusoidal surface with a cavity at the origin (0,0) is represented by:

$$z = -A \cos \left( \frac{2\pi x}{\lambda} \right) \cos \left( \frac{2\pi y}{\lambda} \right) \quad (7)$$

Since it is assumed that the surface roughness is random and independent of orientation, the asperity wavelength  $\lambda$  is the same in both  $x$  and  $y$  dimensions. The amplitude can be related to the average roughness as:

$$A = \frac{\pi^2 R_a}{4}, \quad (8)$$

and to the wavelength and mean normal angle as:

$$\lambda \simeq \frac{4A}{\tan \phi_m} = \frac{\pi^2 R_a}{\tan \phi_m} \quad (9)$$

Physically,  $\lambda$  is the unit cell size for surface cavities; thus, the maximum possible nucleation site density of the sinusoidal surface is  $1/\lambda^2$ . However,  $\lambda$  alone only indicates the spacing of depressions in the surface, but not their shape or depth. Since nucleating cavities

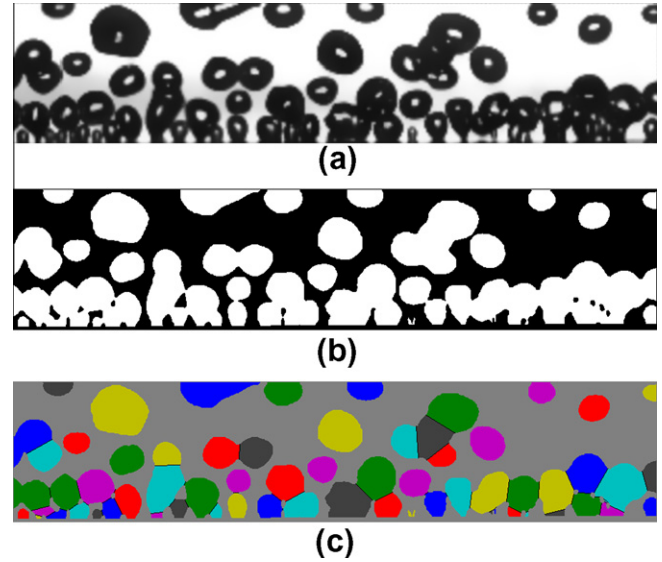


**Fig. 2.** Approximate convex decomposition of bubble objects in an image: (a) original image, (b) binary image after segmentation, and (c) decomposition of objects by the convexity measure of McHale and Garimella [27].

are necessarily points of high surface curvature, a related parameter of interest is the (idealized) maximum surface curvature,  $\kappa_{\text{max}}$ . Combining Eqs. (7) and (9) and maximizing the curvature yields

$$\kappa_{\text{max}} \simeq \frac{\tan^2 \phi_m}{R_a} \quad (10)$$

which is the curvature at the bottom of each idealized sinusoidal cavity, including the one at (0,0).

## 3. Video processing and bubble measurements

Bubble departure statistics were quantified in order to examine the effect of surface roughness. Large, representative sample sets were desirable in order to achieve reasonable levels of statistical significance. Automated measurement of bubble data from the videos was therefore necessary. The video interrogation window, shown in Fig. 2a, was approximately 10 mm long by 2 mm high so that bubble size and history measurements could be performed over a large portion (40%) of the surface. High speed videos of each boiling test condition contained 0.5 s of history, with 2000 frames at a frame rate of 4000 fps. By using short lighting pulses of between about 3 and 6  $\mu\text{s}$  width, the bubbles were very clearly resolved in the images. Significant changes in bubble position and shape occurred only over many successive frames. The temporal resolution of the video allowed all but the very initial stages of bubble growth (less than 250  $\mu\text{s}$ ) to be measured; during this phase of bubble growth the diameters of the nuclei are known to be less than the spatial resolution of the images.

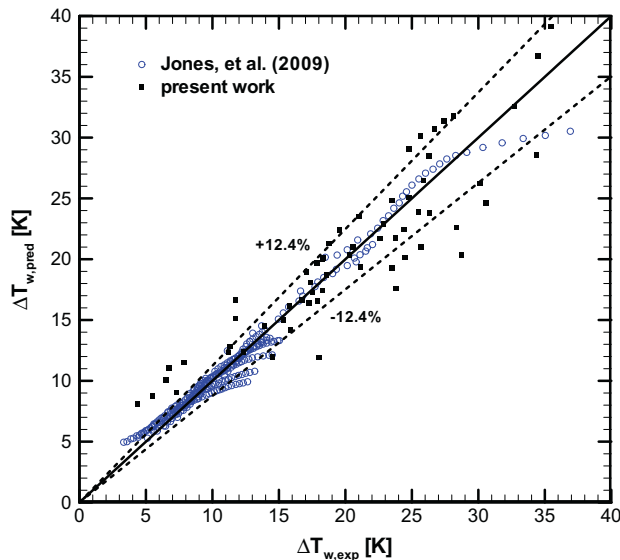


Fig. 3. Correlation of experimental boiling curves assuming the relationship  $h = C_h \cdot q^{0.83}$  provides a basis for comparison independent of heat flux, while introducing relatively little error. MAE for the present data is 12.4%; while for the data of [17], the MAE is 5.2%.

### 3.1. Measurement uncertainty (isolated bubbles)

The spatial image resolution was calculated from identifying features in the bottom and side views and was known to within 0.1%. The uncertainty of the temporal resolution was that of the pulse/delay generator used to synchronize the imaging equipment, 26 ns for this experiment. The video technique was adequate to measure individual bubbles with practical uncertainties of approximately half the spatial and temporal resolution, or 17.2  $\mu\text{m}$  and 125  $\mu\text{s}$ , respectively. The relevant length and time scales for bubble growth and detachment were determined to be around  $L_0 = 600 \mu\text{m}$  and  $t_0 = 5 \text{ ms}$ , respectively. Resulting full-scale measurement uncertainties were therefore approximately 2.9% and 2.5% for the length and time dimensions, respectively.

### 3.2. Image processing challenges and solutions

As discussed previously, the choices of experiment design in this work were dictated by a tradeoff between good heat transfer characteristics and good image quality. The wider the test strip, the lower is the relative heat loss by conduction, but the greater are the bubble overlaps that would appear in images. Even with a heater width as narrow as 400  $\mu\text{m}$ , the number density of bubbles was high enough to make individual bubble identification challenging (“object” versus “objects”). Uncertainty values listed in Section 3.1 were therefore magnified by the degree of bubble object overlap per image frame. A second problem encountered was with image quality. Surface roughness led to non-ideal backlighting conditions, as was also seen in the goniometer images presented in [1]. Thresholding (“object” versus “not object”) was made more difficult by: (1) the common occurrence of a darkened band above the surface for many of the cases, and (2) bright points of backlight transmission and refraction through bubbles. The third major issue in measuring bubbles over a time span was distinguishing a particular bubble in subsequent frames (“object 1” versus “object 2”). Solutions to these three main problems were often complicated by tradeoffs, as a good solution for one problem might introduce further difficulty into another. Rather than conduct a

detailed and tedious optimization study, the following four-step video processing method was developed by trial and error.

#### Step 1: Image filtering for “object” vs. “not object”.

Image intensities were first rescaled on the interval (0,1) in order to heighten contrast between phases. Typically, background “not object” values were white, approaching 1, while bubble “object” intensity values were black, or approaching 0. Unavoidable scattering of light from the roughest surfaces led to uneven background intensity values. Where background values were on the dark end of the interval, the discrete cumulative density function of intensity values over a local spatial window was used to determine the likely values of intensity for objects and background. Intensity values were rescaled on (0,1) according to these probable limits. Bubble edges in small, bright regions were still difficult to distinguish from background, however. Absolute differencing with the previous frame (a type of 3-D filter) highlighted edge regions at the expense of halving the temporal resolution to 250 ms. A second 3-D filter was then applied to avoid increases in apparent bubble size from the differencing operation. Finally a bilateral filter [24,25] was applied to each image frame to help smooth noise within dark and light regions without blurring edges.

#### Step 2: Fuzzy thresholding for “object” vs. “not object”.

Thresholding, typically a binary operation with a set cutoff intensity value, was applied using a fuzzy logic approach. Taking the video as a 3-D array, specific weights between 0 and 1 were given to each voxel based upon its image region characteristics. For example, voxels with intensity values above 0.8 were separated into 6-connected regions. Voxels with unknown “object” status located in the same region as a known “not object” voxel were assigned low “object” status weights of 0.1. “Object” weights of bright regions disconnected from known “not object” regions were increased by 0.2, but if any part of the region was in contact with the surface (location set by manual intervention), “object” weights were decreased by 0.2, and so on. After applying several similar tests of 2-D and 3-D connectivity, the “object” threshold was finally set to 0.5; voxels with “object” values greater than or equal to 0.5 were then set to binary 1, while “object” values below 0.5 were set to binary 0, as depicted in Fig. 2b.

#### Step 3: Approximate convex decomposition for “object” vs. “objects”.

As can be seen in Fig. 2b, multiple objects tended to overlap with each other. 3-D or 2-D morphological region-finding algorithms would fail to distinguish multiple bubbles from each other, and this was the main difficulty encountered in the automatic measurement process. Bubble objects did not occur as uniform, predictable shapes; edge-fitting methods could therefore not be used with good accuracy. 3-D and 2-D watershed transforms, on the other hand, are highly sensitive to marker locations and encounter difficulty in dividing objects along intuitive paths; watershedding was therefore not a good option either. Since bubbles are nearly always convex shapes, multiple bubble “macro-objects” were therefore picked apart using a technique called *approximate convex decomposition* (ACD) [26]. A new robust convexity measure [27] was derived to improve computational efficiency and an ACD algorithm was developed from it. As part of the algorithm, accurate area and perimeter measurements were required for recursively evaluating the macro-objects, which were by definition 4-connected regions. An efficient and robust marching-squares type perimeter estimation algorithm for 4-connected regions [28] was therefore developed. Results of ACD are as shown in Fig. 2c.

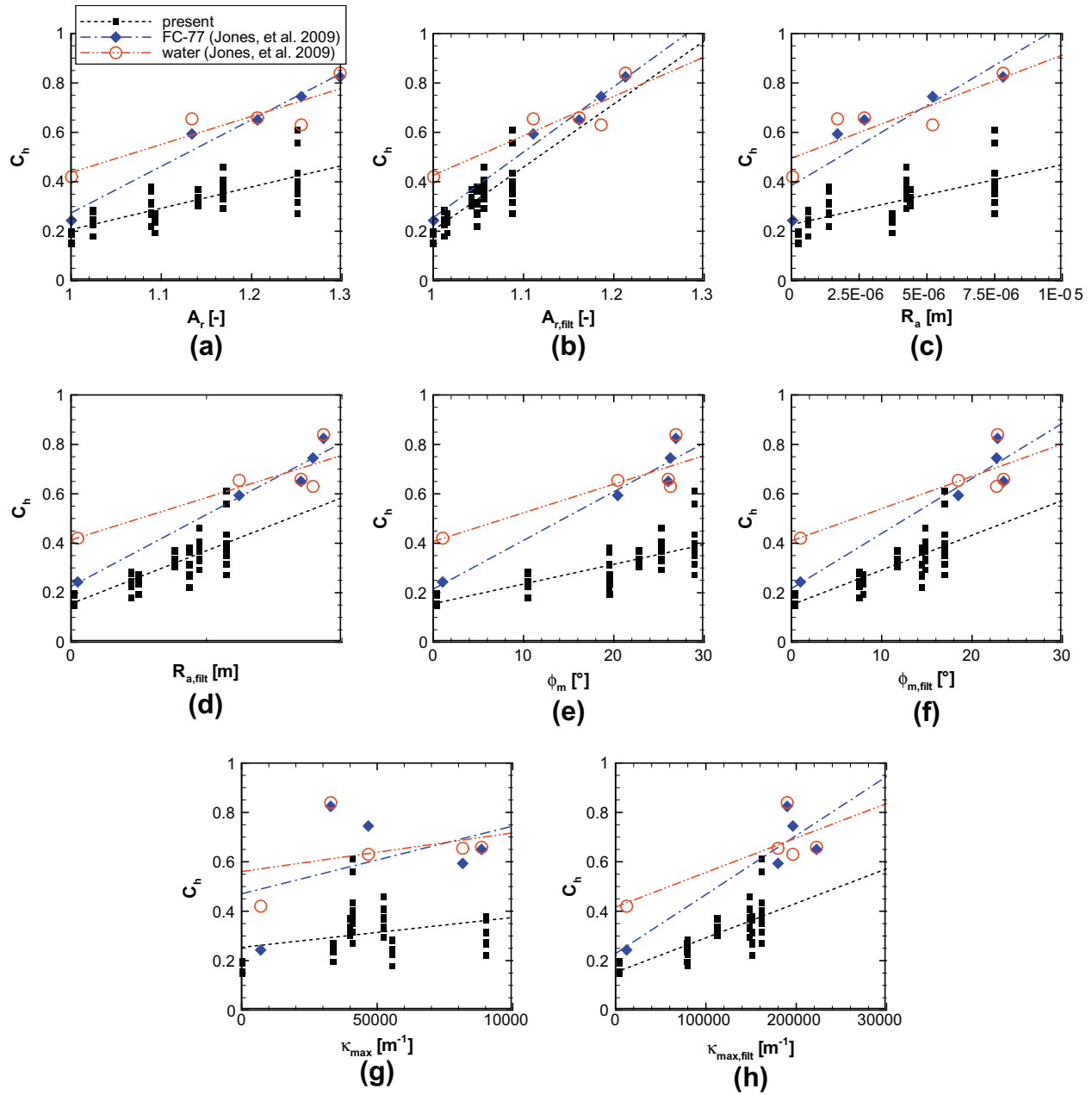


**Fig. 4.** Correlation of  $C_h$  with selected surface parameters. All  $C_h$  data are shown for present work, while only average values are shown for the data of Jones et al. [17]. Correlations are generally better with filtered surface parameters for FC fluids and unfiltered surface parameters for water.

#### Step 4: Particle tracking velocimetry for “object 1” vs. “object 2”.

For particle-laden flows, particle tracking velocimetry (PTV, see, e.g., [29,30]) is an alternative to the well-known particle image velocimetry (PIV) technique. PTV is often more of a brute force approach and less mathematically elegant than PIV, but it is a useful low-error approach whenever the number of objects in the field is low enough and the frame rate is high enough relative to object velocity changes [29]. In PTV, each labeled object in a frame is assigned an expected location and/or size in the next frame, and the distance functions of unlabeled objects from the expected location in that frame are used to find appropriate matches. A major advantage of PTV over PIV is consistent identification of individual objects.

In this work, PTV was applied in successive frames as a double-blind test involving position and not size. Object velocities were low enough to be assumed as zero. A next-frame object

was assigned as a potential match if it was located closer to the current-frame object than any other next-frame object. If the converse was also true, the next-frame object would be assigned the same label as the current-frame object in question. If no matching object was found, the previous frame could be interrogated instead by the same rule.

#### 3.3. Bubble measurements

Once the bubbles were labeled consistently through all frames as described in the previous section, the histories of growth and location of bubbles could be measured. The equivalent bubble diameter at a given point in time was calculated as:

$$D_{eq} = \sqrt{\frac{4A}{\pi}}, \quad (11)$$



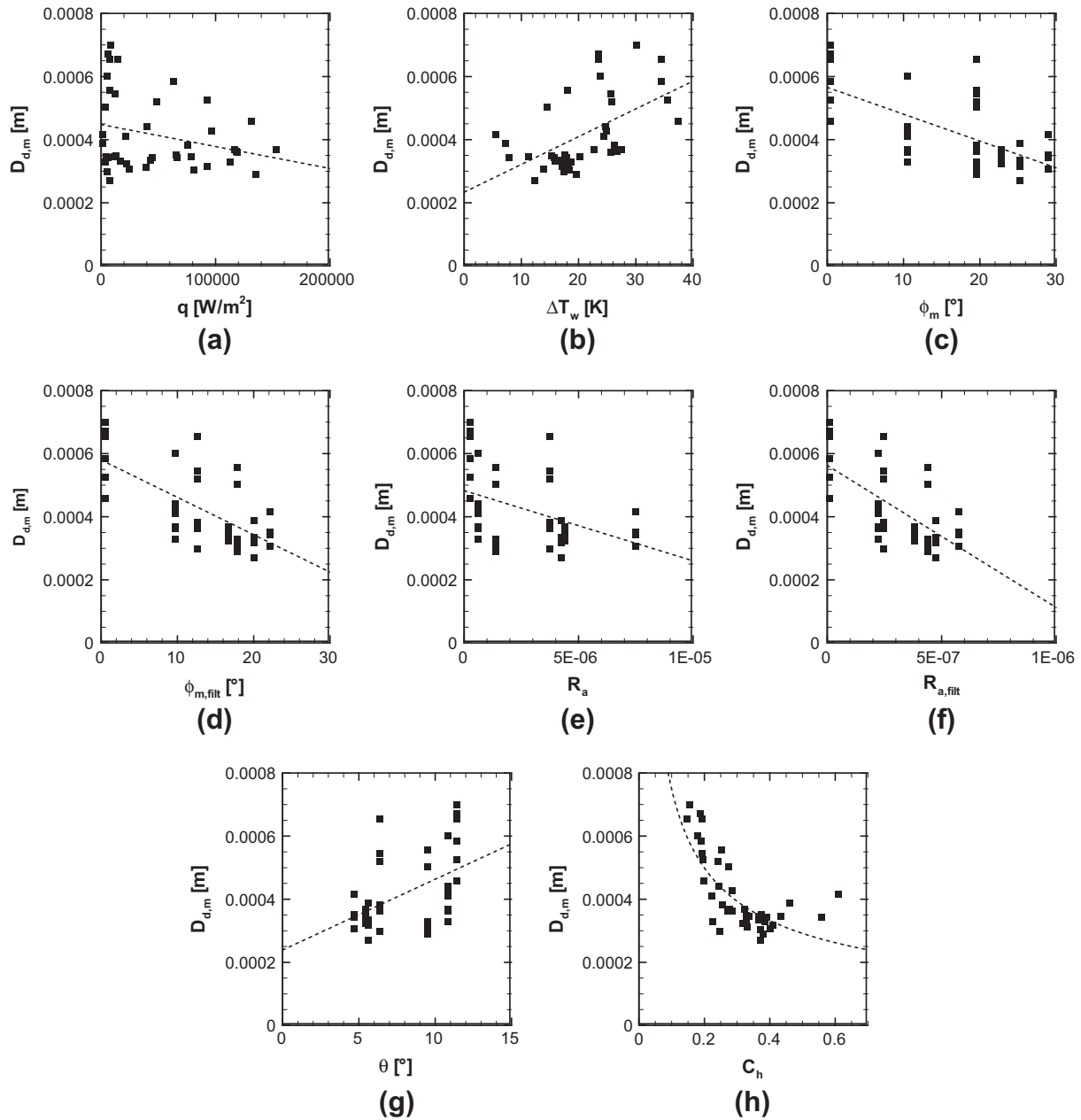


Fig. 5. Experimental trends in mean bubble departure diameter with respect to several correlating variables.

where  $A$  was the planar area of the bubble object in the video. The bubble center position ( $x$  location along surface length,  $y$  location above surface) was calculated as the arithmetic mean of all  $x$  values for the set of pixels in the object, and the mean of all  $y$  values, respectively. Bubble departure was defined to occur when either one of two conditions was met: (1) no pixels in the object were adjacent to the pixels defined as “surface”, or (2) the bubble ceased to exist for more than one frame, a criterion consistent with the 1 skipped frame allowed in the PTV-based object labeling scheme.

Bubble growth periods were calculated as the differences in times associated with the first and last frames of a bubble’s history prior to a departure event. Waiting periods were calculated by incrementing time in reverse, searching for any labeled object containing the same ( $x, y$ ) pixel as the  $x$ -center of a particular bubble in its first frame of existence.

The bubble measurements reported in this work were found to be satisfactory by repeated manual checks. Due to the multiplicity

of interactions and sources of error within the system, however, final uncertainty values were very difficult to quantify precisely. In analyzing results, therefore, we take an approach that assumes significant and unknown variance to be present in measurements.

#### 4. Correlation of data

In this section, the effects of surface roughness on heat transfer and bubble measurement data are examined. Correlation of experimental data with each proposed roughness parameter is attempted. Since all measurements (particularly the bubble measurements) are subject to a degree of uncertainty, and since the data set considered here is rather limited, we do not seek a single unifying correlation for any of the characteristics. Rather, the strength of correlation is expressed in terms of the uncertainty of correlating sample data with one predictor relative to another. It is shown that the

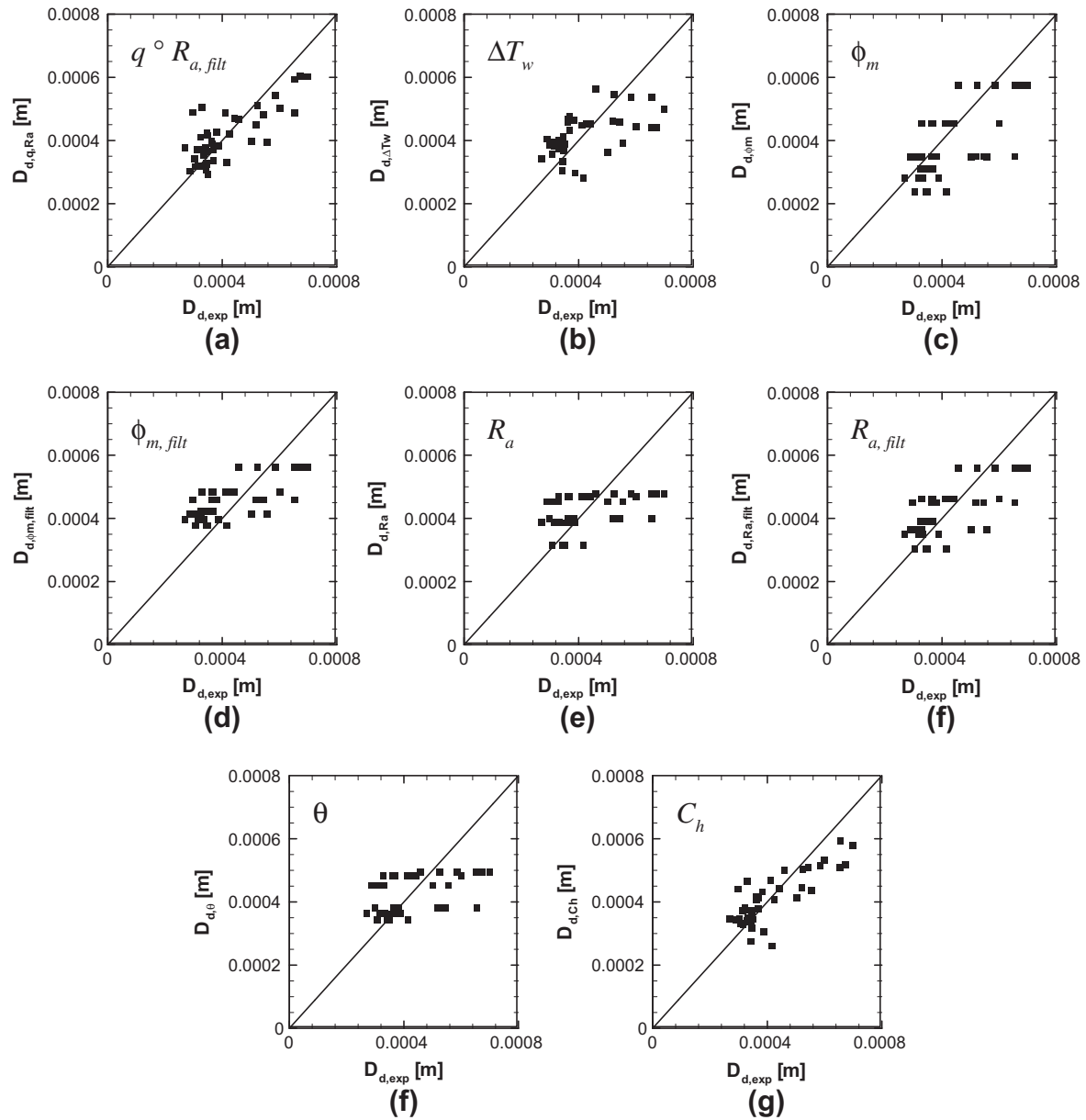


Fig. 6. Comparisons of experimental data and predicted values from curve fits between mean bubble departure diameter and selected variables.

uncertainty is improved for most cases by using the filtered roughness parameters rather than unfiltered parameters, with a few notable exceptions.

#### 4.1. Relative uncertainty

All sample data are assumed to have variances due to measurement error and possibly due to probabilistic dependence upon the predictor(s). Because causal relationships between the data and the parameters of interest are unknown, if they even exist, the correlations are assumed in most cases to be linear. Graphical analysis is known to be a useful tool in identifying correlation forms [31]; so in a few cases, we have included power forms whenever warranted based on scatter plots.

The strength of correlations is compared by one of two methods. First, if all correlations in a particular group are assumed to be single-factor and linear, the linear least-squares regression coefficients are found. The coefficient of determination  $R^2$ , i.e.,

the square of the Pearson product-moment correlation coefficient, and the  $F$ -statistic are calculated [32]. Based on the sample size  $N$  and a linear model with 2 coefficients, there is a single degree of freedom for the mean-square value of the linear model and  $(N - 2)$  degrees of freedom for the mean-square error. The probability  $p$  of making a type-I error – incorrectly rejecting the hypothesis that the two variables share no linear relationship – can then be calculated. The objective at present is not to determine whether the correlation should in fact be first-order linear, but rather the probability of error inherent in the assumption.

The magnitude of a  $p$  value is not in itself very meaningful, but it does provide a basis for comparison between two alternative correlations. Two potential choices of dependent variable,  $V_1$  and  $V_2$ , if from the same sample set, carry identical assumptions when the regression models are calculated in the same way. Therefore the ratio of their two  $p$  values  $p(V_1)/p(V_2)$  gives the relative uncertainty in choosing  $V_1$  as a predictor above  $V_2$ . If the  $p$  ratio is close to 1, the uncertainty associated with correlating with one variable

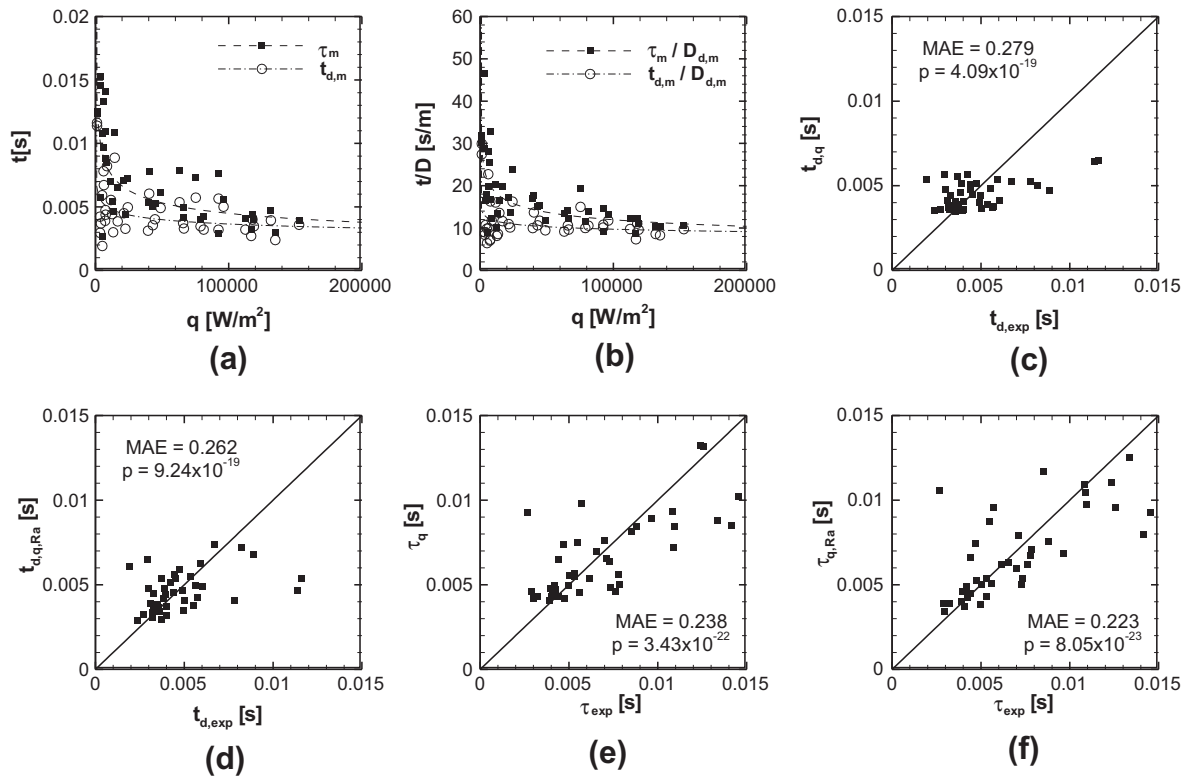


**Fig. 7.** Comparisons of experimental data and predicted values for power curve fits between mean bubble growth period  $t_g$  or total ebullition period  $\tau$  and heat flux, and departure diameter.

above the other is probably negligible, but if it is significantly different from unity, it is clear that that one variable is a superior choice. We arbitrarily choose half an order of magnitude to be a reasonably certain difference only for sake of discussion.

Secondly, if all correlations are either not assumed to be linear or are not single-factor, an alternative method for comparison is needed. In this case, the correlations are all linearized by calculating the mean squares of the model and the error directly. The linearized model must pass through an intercept of zero (expected versus predicted), and the number of degrees of freedom in the error is increased to  $(N - 1)$ . The  $F$ -statistic is again calculated as the ratio of the mean of squares of predicted values and the mean-square error. Magnitudes for  $R^2$  and  $p$  in this type of correlation are essentially meaningless, but the values of  $p$  for different choices of correlating variable have the same scale where  $N$  is the same.

Thus the  $p$  ratio is still a useful measure of relative uncertainty for linearized single-factor correlations. For multiple-factor correlations, however, additional error would be expected due to variation between the multiple factors, and the  $p$  ratio is not a robust estimator of relative uncertainty. Therefore, an unfavorable  $p$  ratio for a multiple-factor model versus an alternate single-factor model may not necessarily indicate greater uncertainty. Conversely, however, if the  $p$  ratio favors the multiple-factor model, the relative uncertainty of the multiple-factor model must be lower.

The  $p$  ratios and/or  $p$  values are examined in the following sections to quantify the relative uncertainties associated with different choices of predictor(s) on boiling heat transfer coefficient and bubble departure diameter. Bubble growth times and total ebullition periods are examined and discussed. Relative uncertainty data are supplemented with mean absolute error (MAE) values calculated as:

$$MAE = \frac{\sum_{i=1}^n |V_{exp} - V_{pred}|}{\sum_{i=1}^n |V_{exp}|} \quad (12)$$

where  $V_{exp}$  and  $V_{pred}$  are the experimental and model-predicted values of the variable in question, respectively. The MAE is a more intuitive measurement of error, although it lacks the statistical meaning of the  $p$  ratio.

#### 4.2. Effect of surface roughness on heat transfer coefficient

Several good correlations [33–36] are available that make use of unfiltered roughness height parameters, with the effect of surface roughness expressed in the form  $h \sim R^m$ . The exponent  $m$  is either a constant or a variable dependent upon reduced pressure, with values that usually fall in the range 0.1–0.2 (typical of water and organic liquids, respectively). To the authors' knowledge, no physical justification has been proposed for  $m \neq 1$ ; rather, it is an empirical trend that agrees satisfactorily with much of the extant data. The success of these correlations in fitting many data sets would seem to depend upon the common existence of a fractal type of roughness in which geometrically similar features occur independent of measurement scale. In the present work, however, this is not a tenable assumption, which can clearly be seen in the SEM photos of Fig. 1 in the companion paper to this work [1].

Correlations often relate the heat transfer coefficient to boiling heat flux in the form  $h = C_h \cdot q^n$  [17], where the exponent  $n$  may vary with fluid and roughness and the coefficient  $C_h$  captures all other factors. For fixed  $n$ , the value of the corresponding coefficient  $C_h$  is an indicator of how boiling curves for different surfaces and fluids compare in terms of wall superheat. Since heat flux values and wall superheats could not be fixed for the present experiments,  $C_h$  is a necessary basis of comparison. Since  $h \sim C_h$ , the effect of a suitable roughness parameter on  $C_h$  is the same as its effect upon  $h$  independent of  $q$ . For the present data, as well as those of Jones et al. [17],  $n = 0.83$  provides a reasonable correlation for all boiling curves. In Fig. 3, best fit values of  $C_h$  are used to correlate

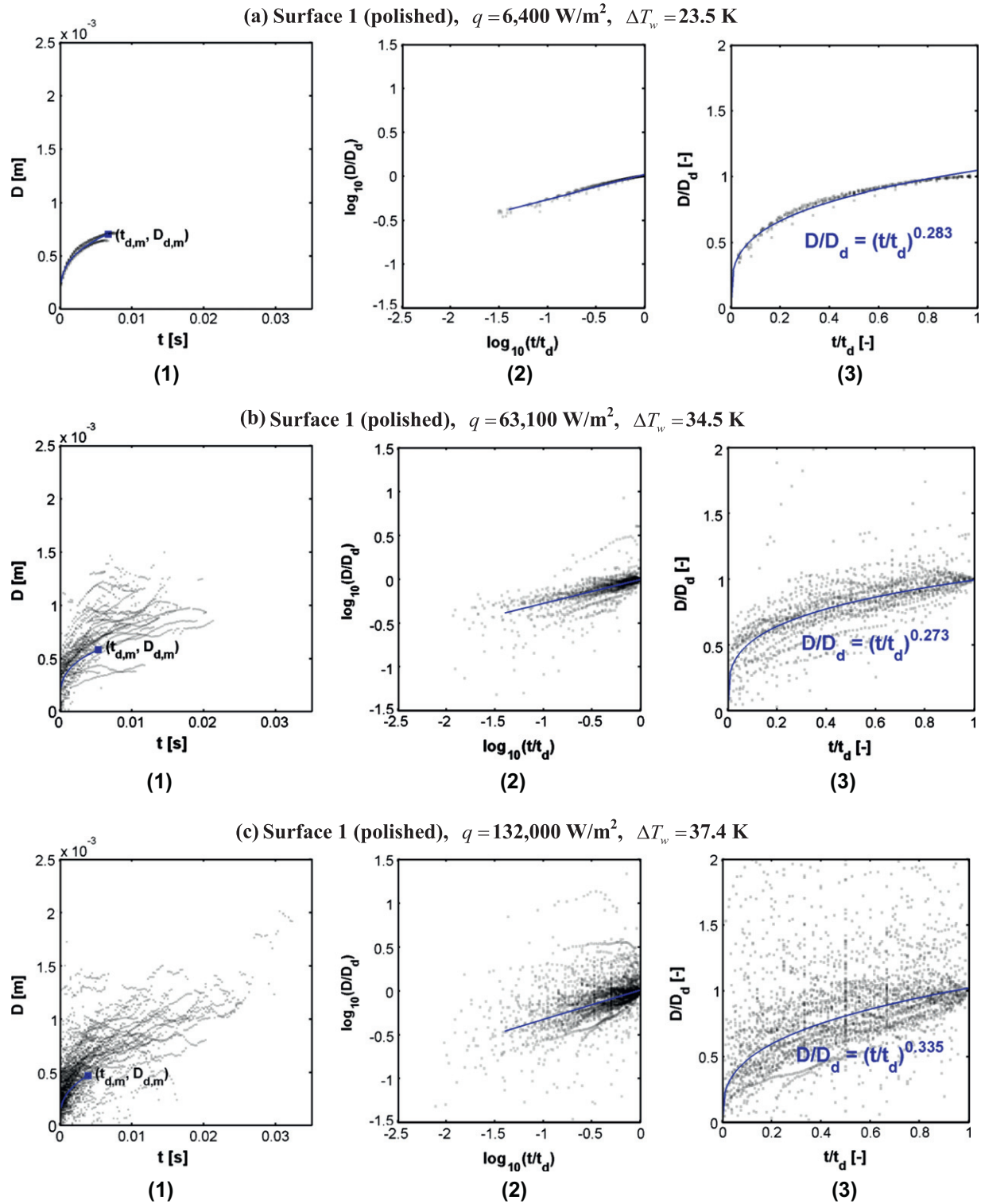


**Fig. 8.** Measured bubble diameters as a function of growth time for surface 1 at (a) low, (b) medium, and (c) high heat fluxes. Chaotic behavior appears to increase with heat flux. The growth relationships shown in panels (2) and (3),  $D \sim t^{1/3}$  remain approximately valid as  $q$  increases.

each boiling curve, and wall superheats from each correlation are compared to the experimental values. The MAE resulting from representing the present boiling curves by  $C_h$  values with the single exponent  $n = 0.83$  is 12.4%. For the pool boiling data of [17] which is included for comparison, the MAE is 5.2%.

In Fig. 4 and the corresponding Table 3, the effects of four surface roughness parameters on  $C_h$  are compared. Both unfiltered and filtered roughness values for each parameter are assessed as predictors. The relationships are all assumed to be linear;  $C_h$  values for the present surfaces 2, 3, 4, and 7 disprove by inspection the

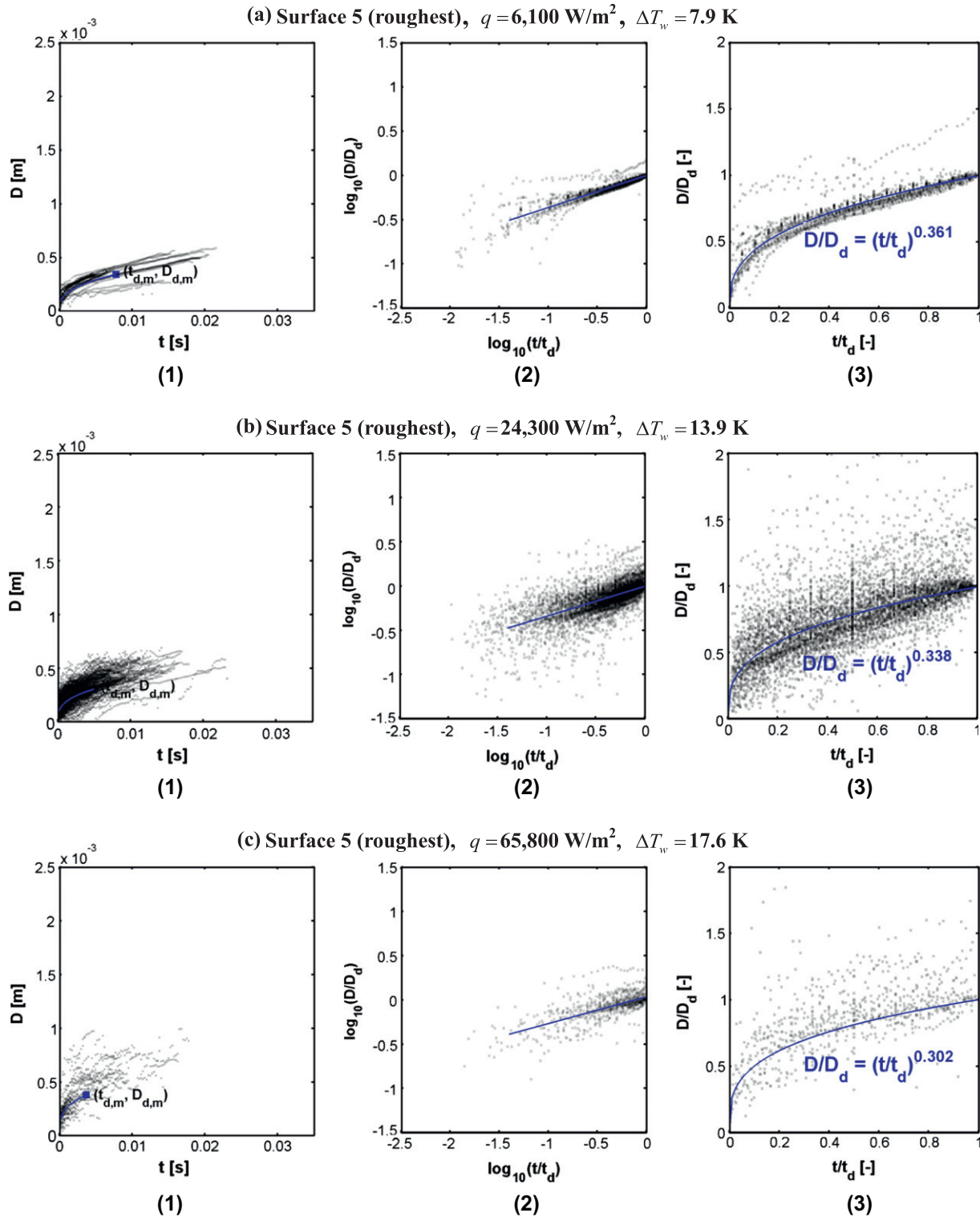


**Fig. 9.** Measured bubble diameters as a function of growth time for surface 5 at (a) low, (b) medium-low, and (c) medium heat fluxes. High nucleation site densities at medium to high heat fluxes inhibited good time domain measurements.

generality of the  $C_h \sim R^m$ ,  $m \neq 1$  model, as may be seen in Fig. 4c. The present data, with only a few  $C_h$  data points for each surface, are all included in the plots. The much larger number of data points from [17] would occlude the plots, so that only the average value of  $C_h$  for each surface is included.

In Table 3, the relative uncertainties of correlation between  $C_h$  and each unfiltered or filtered parameter are compared. Filtered

parameters provide a more certain correlation for FC-72 on ITO ( $\theta = 11.4^\circ$ ,  $\lambda_{cut} = 15.3 \mu\text{m}$ ) and FC-77 on aluminum ( $\theta = 15^\circ$ ,  $\lambda_{cut} = 24.8 \mu\text{m}$ ) according to the proposed theory. The unfiltered parameters provide a better correlation for water on aluminum ( $\theta = 82^\circ$ ,  $\lambda_{cut} = 2.77 \mu\text{m}$ ), since the calculated cutoff wavelength exceeded the dimensions of the available surface maps ( $700 \mu\text{m} \times 500 \mu\text{m}$ ). The  $p$  ratios for filtered versus unfiltered



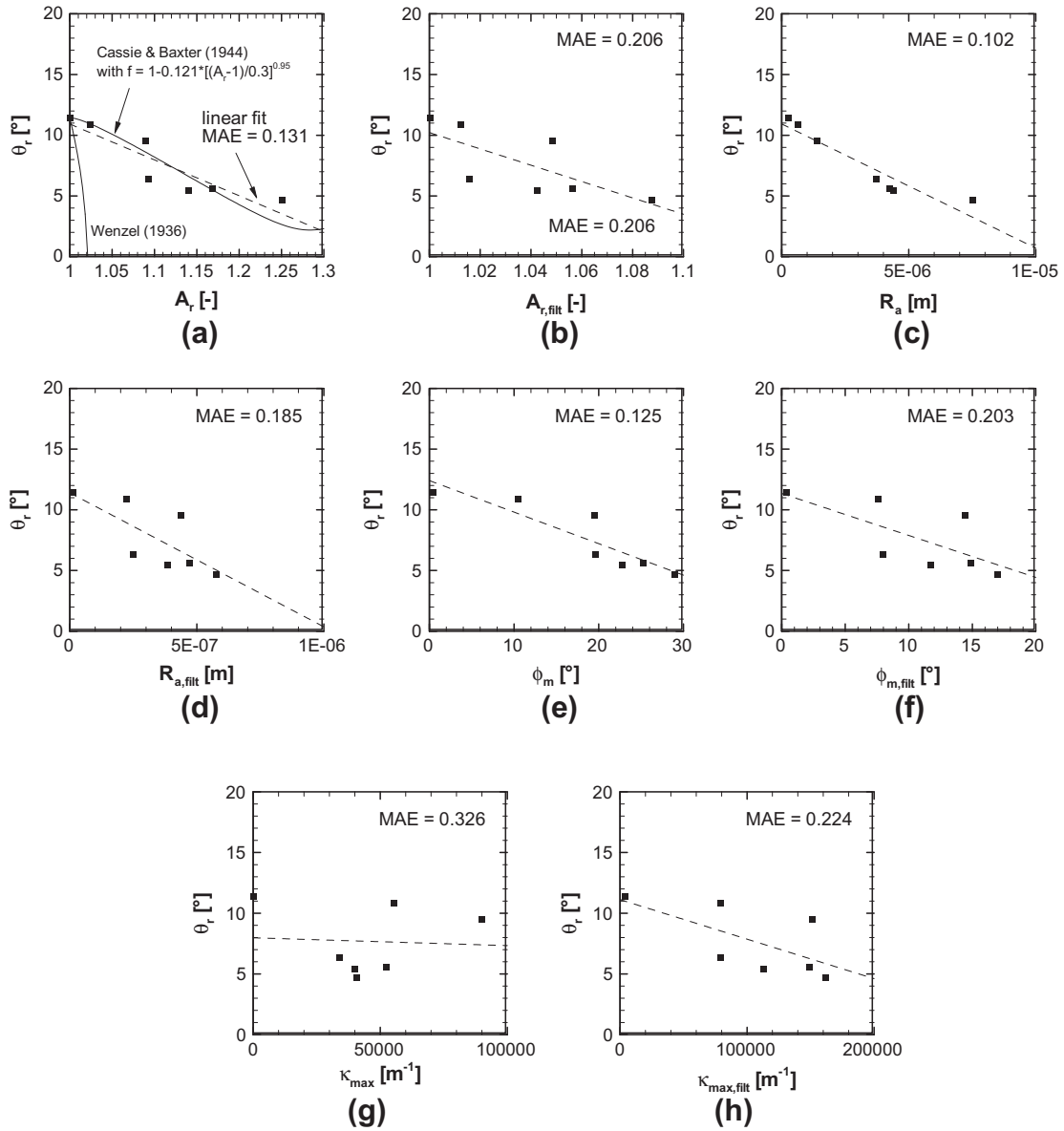


**Fig. 10.** Comparisons of variation of experimental contact angle  $\theta$  with calculated surface parameters. Filtered surface parameters do not generally provide better correlation for wetting.

parameters and each parameter versus  $A_r$  are given in the last two columns of Table 3, respectively.

By  $p$  ratio, the filtered value  $R_{a, \text{fit}}$  provides the lowest correlation uncertainty for the present FC-72 data, followed closely by  $A_{r, \text{fit}}$ . For FC-72, filtered surface parameters all have lower uncertainties than their respective unfiltered counterparts. For FC-77  $A_{r, \text{fit}}$  gives the smallest uncertainty overall and filtered parameters are superior except for  $\phi_m$ . For water  $A_r$  provides the most certain correlation by  $p$ -ratio compared to the other unfiltered parameters, but the filtered parameter  $A_{r, \text{fit}}$  actually performs slightly better. The relative uncertainties of all parameters, filtered or unfiltered, however, are within an order of magnitude. This is likely due to the somewhat unusual scatter in the water data, for which  $C_h$  values at intermediate roughnesses do not precisely follow a logical trend.

For the three combined data sets, the appropriately filtered  $A_r$  appears to be the best choice of correlating parameter for  $C_h$ , and is therefore marked with an asterisk in the table (\*).  $R_a$  (filtered according to the model) is the next best choice, followed by  $\phi_m$ . The idealized maximum surface curvature  $\kappa_{\text{max}}$  appears to be a

poor choice after analysis, although this may note be obvious from the plots.

#### 4.3. Bubble departure diameter, $D_d$

Carey [37] tabulated most of the extant bubble departure diameter correlations. In summary, they fall into three categories: (1) analytical models based on force analyses [19,38,39], (2) analytical models based on thermal analyses [40–42], and (3) semi-empirical models [43–47]. The correlation of Golorin et al. [45] is the only one for which the analysis includes the effect of surface roughness explicitly, but it does not agree well enough with the present data to explore further here. On the whole, the correlations embody many different forms with respect to heat flux, wall superheat, and fluid parameters. Most use  $L_0$  as the primary length scale.

For simplicity we selected linear forms (as shown in Fig. 5) for correlation of the mean measured value of  $D_d$  at different conditions with respect to: (a)  $q$ , (b)  $\Delta T_w$ , (c)  $\phi_m$ , (d)  $\phi_{m, \text{fit}}$ , (e)  $R_a$ , (f)  $R_{a, \text{fit}}$ , and (g)  $\theta_r$ . For the correlation with  $C_h$  in Fig. 5h, there was a tight grouping of data points suggesting a power fit.  $A_r$  was not

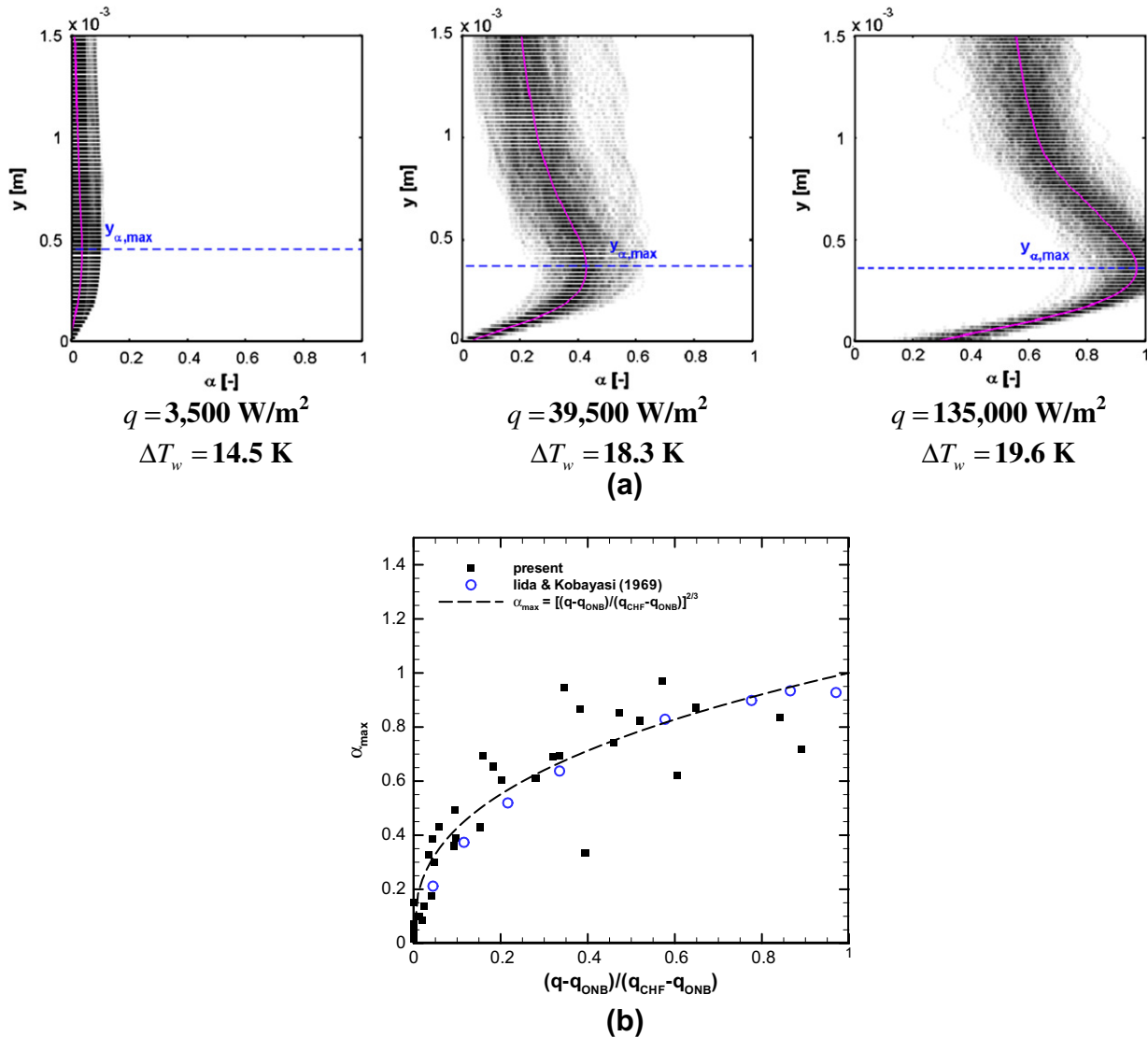


**Fig. 11.** (a) Approximate void fraction distribution above surface 3 at three different heat fluxes. (b) Maximum void fraction can be correlated with normalized nucleate boiling heat flux. The present data (FC-72) compare well with those of Iida and Kobayasi [57] (water).

included in the analysis, since  $R_d$  and  $\phi_m$  gave better fits. It was found that combining the correlations for  $q$  and  $R_{d, \text{filt}}$  better fit the trends within data sets per surface than  $q$  alone. Linearized correlation results are shown in Fig. 6. Relative uncertainties ( $p$ -ratios) and correlation forms for the different variables are listed in Table 4. Overall the correlation of  $D_d$  with the experimental values of  $C_h$  is the best in terms of relative uncertainty. But since this correlation is not fully predictive, we use the correlation with  $R_{d, \text{filt}}$  and  $q$ , panel (a) in Fig. 6, as the basis for comparison.

#### 4.4. Time scale

Bubble growth rates in uniformly superheated liquid fields are well understood and are limited by liquid inertia [48] (typically at the onset of growth), and heat diffusion [49] (typically over most of the life of the bubble for conventional fluids). For a vertically non-uniform superheat considering both limits, analytical solutions for dimensionless growth rates were derived by Mikic et al. [41,50]. Good agreement was obtained with carefully controlled experiments. In fully developed nucleate boiling, however, spatial variations of liquid superheat do not follow a simple 1-D transient

conduction model, and significant departures from the theory are observed.

If the waiting period and growth period are known *a priori*, however, components of boiling heat transfer may be accurately modeled [51]. Predictive correlations for growth rate or ebullition period are therefore of interest. Widely cited correlations [52–54] are usually expressed as the product of ebullition frequency and departure diameter, which results in a characteristic velocity scale.

##### 4.4.1. Bubble growth and ebullition periods, $t_d$ and $\tau$

Mean bubble growth periods  $t_{d,m}$  and mean ebullition periods  $\tau_m$  were obtained from the videos for each test condition. The growth period is defined as the difference in time between the initiation of growth of a bubble and its release from the surface. The ebullition period is defined as the difference in time between the initiation of growth of a bubble and the initiation of growth of the next bubble nucleating from the same cavity.

Trends in bubble growth and ebullition periods with respect to surface parameters were not readily apparent from scatter plots. Surface roughness was not found to affect the bubble growth or ebullition periods significantly. Only trends with  $q$  and  $D_d$  appeared

**Table 3**

Summary of relative uncertainties for linear correlations between  $C_h$  and selected predictive variables. Last 2 columns are  $p$  ratios of unfiltered parameter to filtered parameter, and each parameter to overall best parameter,  $A_r$ , respectively.

Fluid/work	Fig. 4 panels	Correlating variable	MAE	$R^2$	$\frac{p_{un}}{p_{filt}}$	$\frac{p}{p_{A_r}}$
FC-72	(a)	$A_r$	0.148	0.563	38.8	1
	(b)*	$A_{r, filt}$	0.135*	0.616*		
	(c)	$R_a$	0.177	0.413	$1.98 \times 10^5$	0.730
	(d)	$R_{a, filt}$	0.129	0.621		
Present	(e)	$\phi_m$	0.146	0.541	33.7	4.29
	(f)	$\phi_{m, filt}$	0.130	0.596		
	(g)	$\kappa_{max}$	0.216	0.101	$9.06 \times 10^8$	36.6
	(h)	$\kappa_{max, filt}$	0.133	0.563		
FC-77	(a)	$A_r$	0.044	0.971	2.41	1
	(b)*	$A_{r, filt}$	0.032*	0.984*		
	(c)	$R_a$	0.138	0.781	13.5	3.82
	(d)	$R_{a, filt}$	0.045	0.960		
	[17]	$\phi_m$	0.066	0.934	0.545	14.9
	(f)	$\phi_{m, filt}$	0.082	0.902		
	(g)	$\kappa_{max}$	0.268	0.173	12.6	42.9
	(h)	$\kappa_{max, filt}$	0.124	0.806		
Water	(a)*	$A_r$	0.080*	0.795*	1.08	1
	(b)	$A_{r, filt}$	0.078	0.804		
	(c)	$R_a$	0.099	0.735	1.09	1.50
	(d)	$R_{a, filt}$	0.085	0.749		
	[17]	$\phi_m$	0.082	0.731	0.847	1.54
	(f)	$\phi_{m, filt}$	0.085	0.701		
	(g)	$\kappa_{max}$	0.142	0.127	4.90	13.2
	(h)	$\kappa_{max, filt}$	0.098	0.622		

"un" – Unfiltered parameter.

"filt" – Filtered parameter.

\* Appropriately filtered  $A_r$  value provides the most certain correlation over all data and is used as the final basis of comparison.

to show somewhat consistent trends. Fig. 7 shows the approximate power relationships between  $t_{d,m}$  and  $q$  and  $\tau_m$  and  $q$  (Fig. 7a) and  $t_{d,m}/D_{d,m}$  and  $q$  and  $\tau_m/D_{d,m}$  and  $q$  (Fig. 7b). The results of the correlations are shown in Fig. 7c–f. The correlations evaluated are fully predictive in that they accept known or controllable parameters as independent variables. Those including the departure diameter – Fig. 7d and f – are based on values of  $D_d$  predicted by the present best-fit correlation with  $q$  and  $R_{a, filt}$  as expressed in Table 4 row (a). MAE values are lower for the correlations including  $D_d$ . The  $p$  ratio for correlating  $t_d$  with  $q$  and predicted  $D_d$  [panel (d)] versus with  $q$  alone [panel (c)] is about 2, but this is not significant considering the variance introduced by the additional factor. The  $p$  ratio for correlating  $\tau_d$  with  $q$  and predicted  $D_d$  [letter (e)] versus with  $q$  alone is less than 0.25, and is therefore a much less uncertain correlation form. Correlations between  $t_d$  or  $\tau_d$  and  $D_d$  take the form of a representative velocity and therefore agree qualitatively with the cited literature [52–54].

#### 4.4.2. Bubble growth curves

Comparison and discussion of experimental single-bubble growth rates from a number of studies was provided by Lee et al. [42]. They developed a semi-analytical correlation including both the inertially controlled growth and thermally controlled growth regimes and fit the correlation to a large set of experimental data. They found that, in the thermally limiting case (which from their analysis makes up the final 95% of the growth period), the extant data for a variety of fluids could be correlated well in the form  $D^* \sim (t^*)^a$ , where the asterisks indicate normalized quantities and the value of the exponent  $a$  could vary between 1/3 and 1/5. A fundamental issue with the extant data is that it is based on single isolated bubbles (characteristic of low heat fluxes or very smooth surfaces) and/or very small data sets.

In the present work bubble growth curves for all test conditions and surfaces followed a similar relationship between diameter and time when each bubble's growth curve was normalized by the

**Table 4**

Summary of correlations between  $D_d$  and selected variables.

Fig. 6 panel	Correlating variable(s)	Predictive?	Form of Eqn.	MAE	F statistic	$\frac{p}{p_{q \cdot R_{a, filt}}}$
(a)*	$q \circ R_{a, filt}$	Yes	$D_d = (D_{d0} - a \cdot R_{a, filt})(b - c \cdot q)$	0.137	1313	1
(b)	$\Delta T_w$	Partial	$D_d = a \cdot \Delta T_w + D_{d0}$	0.196	763	$4.38 \times 10^4$
(c)	$\phi_m$	Yes	$D_d = D_{d0} - a \cdot \phi_m$	0.444	559	$1.80 \times 10^7$
(d)	$\phi_{m, filt}$	Yes	$D_d = D_{d0} - a \cdot \phi_{m, filt}$	0.419	946	653
(e)	$R_a$	Yes	$D_d = D_{d0} - a \cdot R_a$	0.300	661	$7.21 \times 10^5$
(f)	$R_{a, filt}$	Yes	$D_d = D_{d0} - a \cdot R_{a, filt}$	0.176	970	403
(g)	$\theta$	Yes	$D_d = a \cdot \theta + D_{d0}$	0.423	700	$2.35 \times 10^5$
(h)	$C_h$	No	$D_d = a \cdot (C_h)^{-b}$	0.136	1379	0.376

\*  $p$  Ratios are relative to best predictive correlation, (a).

values of its individual  $D_d$  and  $t_d$  values. Bubble growth charts are shown in Figs. 8 and 9 for the smooth surface 1 and rough surface 5, respectively. Three heat fluxes are shown for each surface. In Fig. 8, the entire range of  $q$  from just above boiling incipience to just below CHF is shown in subfigures (a)–(c). Each consists of plots showing: (1) the dimensional growth curve in units of bubble diameter (in m) and time (in s), (2) the log–log plot of normalized diameter versus normalized time, including the best power fit line, and (3) the linear normalized plot highlighting the general goodness of the fit. Also in plots (1), the average bubble growth curve is superposed on the data. The average departure diameter and time curves may visually appear to underpredict the data, but this is due to the influence of bubbles with lifetimes cut short by mergers with neighboring bubbles.

In Fig. 9, the range of  $q$  spans from just above boiling incipience to about half the value at CHF. Beyond this heat flux value, the nucleation site density became so high that the video processing code was unable to distinguish many bubbles over their entire growth lifetimes. A comparison of curve fits for all the data reveals the average value of the growth exponent  $a$  to be approximately 1/3. For some high heat flux conditions in which the growth of the average bubble was terminated by mergers prior to liftoff, the value of  $a$  is increased somewhat to approximately 0.4. For very some very low heat flux conditions, nucleation sites with large waiting times experienced a growth exponent of up to 1/2. Based on the work of Mikic and Rohsenow [41] and Lee et al. [42], the variation of  $a$  with waiting time is likely due to the increase in temperature field uniformity with time; a value of  $a = 1/2$  is in perfect agreement with the uniform temperature field solution of Plesset and Zwick [49].

#### 4.5. Other trends

Two other important trends were observed from the present experimental study. First, increased surface roughness was accompanied by a decrease in the receding contact angle  $\theta_r$ . Second, the maximum void fraction above the boiling surface was found to correlate well with heat flux.

##### 4.5.1. Effect of surface roughness on contact angle

Variation in measured contact angle  $\theta_r$  with surface roughness was compared (Fig. 10) for the four roughness parameters explored in this work. It was found that the Wenzel [55] model based on area ratio was not a good predictor of rough surface contact angles. The Cassie–Baxter [56] model was not much better, following the apparent linear decrease in contact angle with increasing area ratio only when the contact factor  $f$  was fit as shown in the Fig. 10a. The best correlation was a linear relationship with  $R_a$ . Filtered surface parameters did not produce consistent trends in contact angle, suggesting that the roughness measure of importance for wetting is not closely related to that for bubble nucleation.

##### 4.5.2. Vertical distribution of average void fraction above surface, $\alpha$

The vertical distribution of time-averaged void fraction above the heater surface was obtained as a by-product of the bubble measurement code. Since positions and equivalent diameters of the bubbles were known at each time step, the approximate local void fraction could be calculated. It was assumed that each bubble was approximately spherical and located directly above the test strip center line at position  $y$ , with radius equal to  $D_{eq}/2$ . Then the fraction of projected heater area occupied by vapor at each height  $y$  was determined by subtracting the circular area of each bubble intersecting the  $y$ -plane. Bubble overlaps (vapor spaces accounted twice) were approximately canceled out by the unaccounted vapor space occurring outside the projected heater area. The void fraction for each height  $y$  was then time-averaged across

all video frames. Resulting vertical distributions of void fraction are shown in Fig. 11a. Scatter data reflect the contribution of individual frames. The time-averaged void fraction as a function of height is superposed as a solid magenta line.

The height at which the maximum value of void fraction  $\alpha_{max}$  occurs is indicated with a dashed line. The maximum void fraction values determined for the present study overall agree well with those of Iida and Kobayasi [57], shown in Fig. 11b, when the value of heat flux is normalized as:

$$q^* \equiv \frac{q - q_{ONB}}{q - q_{CHF}} \quad (13)$$

The combined data sets suggest the following simple correlation, which is based on data for both water [57] and FC-72 (present work):

$$\alpha_{max} = (q^*)^{2/3} \quad (14)$$

Eq. (14) requires further experimental validation. Its behavior at the extreme limits are correct: clearly  $\alpha_{max}$  must be equal to zero at the point of boiling incipience and close to one at the point of surface dryout. Surface roughness was not found to have a definite effect on  $\alpha_{max}$ . Although the three visible outliers below the curve in Fig. 11b pertain to surface 1, reduced calculated  $\alpha_{max}$  values could result from the measurement assumption that bubble overlaps offset unaccounted void space in this case.

## 5. Conclusions

In a companion paper [1], it was shown through a review of the literature and experimental measurements that the effects of surface roughness on nucleate boiling are not completely understood. Quantitative and qualitative differences between nucleate boiling from smooth and rough surfaces were demonstrated. In the present work, the experimental data from [1] were analyzed in depth in order to identify physical reasons for those differences. Surface roughness was analyzed in terms of its relationship to bubble growth and departure. It was shown that filtering the surface using a cutoff wavelength equal to the theoretical base diameter of an emergent bubble can yield appropriate measures of surface roughness as it relates to boiling. While the propriety of using this length scale for filtering must be verified against further experimental evidence, it is based on sound principles and is supported by three data sets. Statistical analysis was performed in order to determine which surface roughness parameters and other predictive quantities could correlate to boiling heat transfer with the lowest uncertainty. It was found that the area ratio  $A_r$ , defined as total surface area divided by planar base area, filtered by the calculated cutoff wavelength appropriate for a specific fluid, provides the most certain correlation for heat transfer coefficients over all the data considered. The filtered  $R_a$  value yielded the most certain correlation for the heat transfer and bubble ebullition data from the present facility. Bubble departure diameter was found to correlate reasonably well with heat flux and  $R_{a, \text{filt}}$ . Bubble ebullition and growth periods was found to correlate well with a combination of heat flux and departure diameter (as predicted by the surface roughness). Bubble growth curves for all test conditions were well represented by the normalized relationship  $D^* \sim (t^*)^{1/3}$ . Finally, void fraction above the surface was correlated with normalized heat flux for these data and for water by  $\alpha_{max} = (q^*)^{2/3}$ .

## Acknowledgments

Financial support for this work was provided by the Indiana 21st Century Research and Technology Fund and the Cooling Technologies Research Center at Purdue University. Ms. Suchismita

Sarangi assisted in construction and operation of the experimental facility. The authors also thank Northrop Grumman Corporation for donating FC-72 working fluid.

## References

- [1] J.P. McHale, S.V. Garimella, Nucleate boiling from smooth and rough surfaces – Part 1: fabrication and characterization of an optically transparent heater-sensor substrate with controlled surface roughness, *Experimental Thermal Fluid Science* 44 (2013) 456–467.
- [2] Y. Qi, J.F. Klausner, R. Mei, Role of surface structure in heterogeneous nucleation, *International Journal of Heat and Mass Transfer* 47 (2004) 3097–3107.
- [3] D. Gorenflo, A. Luke, E. Danger, Interactions between heat transfer and bubble formation in nucleate boiling, in: *Proceedings of 11th International Heat Transfer Conference*, Kyongju, 1998, pp. 149–174.
- [4] A. Luke, E. Baumhögger, P. Scheunemann, 3-Dimensional description of the microstructure of heated surfaces in nucleate pool boiling, *Multiphase Science & Technology* 12 (2000) 136–151.
- [5] A. Majumdar, C. Tien, Fractal characterization and simulation of rough surfaces, *Wear* 136 (1990) 313–327.
- [6] R. Fong, G. McRae, C. Coleman, T. Nitheanandan, D. Sanderson, Correlation between the critical heat flux and the fractal surface roughness of Zirconium alloy tubes, *Journal of Enhanced Heat Transfer* 8 (2001) 137–146.
- [7] S.R. Yang, Z.M. Xu, J.W. Wang, X.T. Zhao, On the fractal description of active nucleation site density for pool boiling, *International Journal of Heat and Mass Transfer* 44 (2001) 2783–2786.
- [8] B. Yu, P. Cheng, A fractal model for nucleate pool boiling heat transfer, *Journal of Heat Transfer* 124 (2002) 1117–1124.
- [9] W.M. Rohsenow, A method of correlating heat transfer data for surface boiling of liquids, *Transactions of the ASME* 74 (1952) 969–976.
- [10] R. Benjamin, A. Balakrishnan, Nucleate pool boiling heat transfer of pure liquids at low to moderate heat fluxes, *International Journal of Heat and Mass Transfer* 39 (1996) 2495–2504.
- [11] R. Judd, K. Hwang, A comprehensive model for nucleate pool boiling heat transfer including microlayer evaporation, *Journal of Heat Transfer* 98 (1976) 623–629.
- [12] K. Torikai, M. Hori, M. Akiyama, T. Kobori, H. Adachi, Boiling heat transfer and burn-out mechanism in boiling-water cooled reactors, in: *Proceedings of Third United Nations International Conference on the Peaceful Uses of Atomic Energy*, 1964, Paper No. 28/P580.
- [13] B.B. Mikic, W.M. Rohsenow, A new correlation of pool-boiling data including the effect of heating surface characteristics, *Journal of Heat Transfer* 91 (1969) 245–250.
- [14] C. Han, P. Griffith, The mechanism of heat transfer in nucleate boiling. Parts I and II, *International Journal of Heat and Mass Transfer* 8 (1965) 887–914.
- [15] C.H. Wang, V.K. Dhir, Effect of surface wettability on active nucleation site density during pool boiling of saturated water, *Journal of Heat Transfer* 115 (1993) 659–669.
- [16] V. Sathyamurthi, D. Banerjee, H. Sakamoto, J. Kim, Measurement of the fractal order of wall void fraction during nucleate boiling, *International Journal of Heat and Fluid Flow* 29 (2008) 207–218.
- [17] B.J. Jones, J.P. McHale, S.V. Garimella, The influence of surface roughness on nucleate pool boiling heat transfer, *Journal of Heat Transfer* 131 (2009) 121009.
- [18] F. Bashforth, J.C. Adams, An Attempt to Test the Theories of Capillary Action: By Comparing the Theoretical and Measured Forms of Drops of Fluid, University Press, 1883.
- [19] W. Fritz, Berechnung des maximalvolumen von dampfblasen, *Physikalische Zeitschrift* 36 (1935) 379–388.
- [20] S. Hartland, R. Hartley, *Axisymmetric Fluid–Liquid Interfaces*, Elsevier, Amsterdam, 1976.
- [21] M. Owen, *Practical Signal Processing*, Cambridge University Press, New York, 2007.
- [22] The Mathworks Inc., MATLAB version 7.8.0, Natick, Massachusetts, 2009.
- [23] A.V. Oppenheim, R.W. Schaffer, J.R. Buck, *Discrete-Time Signal Processing*, Prentice-Hall, Upper Saddle River, NJ, 1999.
- [24] C. Tomasi, R. Manduchi, Bilateral filtering for gray and color images, in: *Sixth. International (Ed.), Conference on Computer Vision*, Bombay, IEEE, 1998, pp. 839–846.
- [25] D.R. Lanman, *bfilter2.m*, Brown University, 2006.
- [26] J.M. Lien, N.M. Amato, Approximate convex decomposition of polygons, *Computational Geometry* 35 (2006) 100–123.
- [27] J.P. McHale, S.V. Garimella, New measures for convexity and concavity of objects, pockets, and vertices based on circularity, *Pattern Recognition Letters*, (submitted for publication).
- [28] J.P. McHale, S.V. Garimella, Robust LUT-based perimeter estimation for 4-connected binary objects, (in preparation).
- [29] K. Ohmi, H.-Y. Li, Particle-tracking velocimetry with new algorithms, *Measurement Science and Technology* (2000) 603–616.
- [30] D. Broder, M. Sommerfeld, Planar shadow image velocimetry for the analysis of the hydrodynamics in bubbly flows, *Measurement Science and Technology* 18 (2007) 2513–2528.
- [31] B.M. Ayyub, R.H. McCuen, *Probability, Statistics, and Reliability for Engineers and Scientists*, Chapman & Hall/CRC, Boca Raton, FL, 2003.
- [32] D. Schiff, R.B. D'Agostino, *Practical Engineering Statistics*, Wiley-Interscience, New York, 1996.
- [33] M. Cooper, Saturation nucleate pool boiling: a simple correlation, in: *1st UK National Conference on Heat Transfer*, 1984, pp. 785–793.
- [34] K. Nishikawa, Y. Fujita, H. Ohta, S. Hidaka, Effects of system pressure and surface roughness on nucleate boiling heat transfer, *Memoirs of the Faculty of Engineering, Kyushu University* 42 (1982) 95–111.
- [35] D. Gorenflo, Pool Boiling, in: *VDI Heat Atlas*, VDI Verlag, Dusseldorf, 1993.
- [36] W. Leiner, Heat transfer by nucleate pool boiling-general correlation based on thermodynamic similarity, *International Journal of Heat and Mass Transfer* 37 (1994) 763.
- [37] V.P. Carey, *Liquid–Vapor Phase-Change Phenomena: An Introduction to the Thermophysics of Vaporization and Condensation*, Hemisphere Publishing Corp., Washington, DC, 1992.
- [38] A. Hatton, I. Hall, Photographic study of boiling on prepared surfaces, in: *Proceedings of 3rd International Heat Transfer Conference*, 1966, pp. 24–37.
- [39] E. Ruckenstein, A physical model for nucleate boiling heat transfer from a horizontal surface, *Buletinul Institutului Politehnic Bucuresti (Romania)* 23 (1961) 79–88.
- [40] N. Zuber, *Hydrodynamic Aspects of Boiling Heat Transfer*, AECU-4439, California. Univ., Los Angeles; and Ramo-Wooldrige Corp., Los Angeles, 1959.
- [41] B.B. Mikic, W.M. Rohsenow, Bubble growth rates in non-uniform temperature field, *Progress in Heat and Mass Transfer* 2 (1969) 283–293.
- [42] H.C. Lee, B.D. Oh, S.W. Bae, M.H. Kim, Single bubble growth in saturated pool boiling on a constant wall temperature surface, *International Journal of Multiphase Flow* 29 (2003) 1857–1874.
- [43] R. Cole, W. Rohsenow, Correlation of bubble departure diameters for boiling of saturated liquids, *Chemical Engineering Progress Symposium Series* 65 (1969) 211–213.
- [44] R. Cole, H.L. Shulman, Bubble departure diameters at subatmospheric pressures, *Chemical Engineering Progress* 62 (1966) 6–16.
- [45] V. Golorin, B. Kol'chugin, E. Zakharova, Investigation of the mechanism of nucleate boiling of ethyl alcohol and benzene by means of high-speed motion-picture photography, *Heat Transfer – Soviet Research* 10 (1978) 79–98.
- [46] S. Kutateladze, I. Gogonin, Growth rate and detachment diameter of a vapor bubble in free convection boiling of a saturated liquid, *High Temperature* 17 (1980) 667–671.
- [47] M.K. Jensen, G.J. Memmel, Evaluation of bubble departure diameter correlations, in: *Proceedings of the Eighth International Heat Transfer Conference*, 1986, pp. 1907–1912.
- [48] Lord. Rayleigh, On the pressure developed in a liquid during the collapse of a spherical cavity, *Philosophical Magazine* 34 (1917) 94–98.
- [49] M.S. Plesset, S.A. Zwick, The growth of vapor bubbles in superheated liquids, *Journal of Applied Physics* 25 (1954) 493–500.
- [50] B.B. Mikic, W.M. Rohsenow, P. Griffith, On bubble growth rates, *International Journal of Heat and Mass Transfer* 13 (1970) 657–666.
- [51] S. Moghaddam, K. Kiger, Physical mechanisms of heat transfer during single bubble nucleate boiling of FC-72 under saturation conditions. II: Theoretical analysis, *International Journal of Heat and Mass Transfer* 52 (2009) 1295–1303.
- [52] M. Jakob, W. Fritz, Versuche über den verdampfungsvorgang, *Forschung auf dem Gebiete des Ingenieurwesens* 2 (1931) 435–447.
- [53] F.N. Peebles, H.J. Garber, Studies on motion of gas bubbles in liquids, *Chemical Engineering Progress* 49 (1953) 88–97.
- [54] H.J. Ivey, Relationships between bubble frequency, departure diameter and rise velocity in nucleate boiling, *International Journal of Heat and Mass Transfer* 10 (1967) 1023–1040.
- [55] R.N. Wenzel, Resistance of solid surfaces to wetting by water, *Industrial & Engineering Chemistry* 28 (1936) 988–994.
- [56] A. Cassie, S. Baxter, Wettability of porous surfaces, *Transactions of the Faraday Society* 40 (1944) 546–551.
- [57] Y. Iida, K. Kobayasi, Distributions of void fraction above a horizontal heating surface in pool boiling, *Bulletin of JSME* 12 (1969) 283–290.